A unified model for the permeability, electrical conductivity and streaming potential coupling coefficient in variably saturated fractured media

Luong Duy Thanh, Nguyen van Nghia, Phan van Do, Pham Tien Du, Damien Jougnot

A unified model for the permeability, electrical conductivity and streaming potential coupling coefficient in variably saturated fractured media

Luong Duy Thanh[1], **Nguyen Van Nghia***[1], **Phan Van Do**[1], **Pham Tien Du**[1], **Damien Jougnot**[2]

[1] *Thuyloi University, 175 Tay Son, Dong Da, Hanoi, Vietnam*

[2] *Sorbonne Université, CNRS, EPHE, UMR 7619 Metis, F-75005, Paris, France*

* *Email: nghia_nvl@tlu.edu.vn*

(October 13, 2022)

ABSTRACT

We present a new unified model for the permeability, electrical conductivity, and streaming potential coupling coefficient in variably saturated fractured media. For those, we conceptualize the fractured medium as a partially saturated bundle of parallel capillary slits with varying sizes. We assume that the fracture size distribution of the corresponding medium follows a fractal scaling law, which allows us establish a pressure head-saturation relationship based on the Laplace equation. We first describe the flow rate, the conduction current, and the electrokinetic streaming current within a single fracture. Then, we upscale these properties at the scale of an equivalent fractured media partially saturated in order to obtain the relative permeability, the electrical conductivity and the streaming potential coupling coefficient. The newly proposed model explicitly depends on pore water chemistry, interface properties, microstructural parameters of fractured media, and water saturation. Model predictions are in good agreement with both experimental and simulated data and with another model from the literature. The results of this work constitute a useful framework to estimate hydraulic properties and monitor water flow in fractured media.

Keywords: Fractured media; Streaming potential; Electrical conductivity; Permeability; Fractal

INTRODUCTION

The streaming potential (SP) is a contribution to the self-potential signal that is generated by water flow in porous media. Due to the sensitivity of the SP method to subsurface water flow, the SP technique has drawn an increasing attention to find or track underground water in aquifers or reservoirs (e.g., Revil et al., 2012; Parsekian et al., 2015; Binley et al., 2015). This technique has been used for identifying and monitoring subsurface water flow (e.g., Jouniaux et al., 1999; Fagerlund and Heinson, 2003; Titov et al., 2005; Aizawa et al., 2009), monitoring geothermal and volcanic areas (e.g., Corwin and Hoover, 1979; Finizola et al., 2004; Mauri et al., 2010; Soueid Ahmed et al., 2018; Grobbe and Barde-Cabusson, 2019), mapping areas influenced by a contaminant plume (e.g., Martinez-Pagan et al., 2010; Naudet et al., 2003; Roy, 2022), monitoring water flow in the vadose zone (e.g., Doussan et al., 2002; Jougnot et al., 2015; Hu et al., 2020) or eco-hydrology (e.g., Voytek et al., 2019). The SP technique can be applied to estimate hydrogeological parameters of the aquifer (e.g., Jardani et al., 2007; Straface et al., 2010; Revil and Jardani, 2013).

Fractured rocks are ubiquitous in the environment and they play a major role in a wide range of geoscience issues, such as groundwater flow and contaminant transport (e.g., Neuman, 2005; Medici et al., 2019), hydraulic fracturing (e.g., Osiptsov, 2017; Peshcherenko et al., 2022), storage of CO_2 and nuclear waste (e.g., Bodvarsson et al., 1999; Wang and Hudson, 2015; Ren et al., 2017), geothermal production (e.g., Murphy et al., 1981; Patterson et al., 2020). Geophysical methods offer a variety of tools to obtain information on subsurface structure and physical properties of fractured rocks. Examples of those methods include the electrical conductivity imaging (e.g., Stesky, 1986; Shen et al., 2009; Roubinet and Irving, 2014), seismic technique (e.g., Herwanger et al., 2004; Li, 1997; Clair et al., 2015), or the self potential technique (e.g., Fagerlund and Heinson, 2003; Wishart et al., 2006; Maineult et al., 2013). It is shown that numerical approaches are effective to characterize fractured media (e.g., Roubinet and Irving, 2014; Roubinet et al., 2016; Demirel

et al., 2018; Haas et al., 2013; DesRoches et al., 2018; Jougnot et al., 2020). However, to the best of our knowledge, there are only few analytical models for fractured rocks in the literature. For example, Thanh et al. (2021) proposed a model for the electrical conductivity and streaming potential coupling coefficient in fractured media under saturated conditions using a capillary bundle model following the fractal scaling law. Guarracino and Jougnot (2022) presented a model to predict the effective excess charge density for fully and partially water saturated fractured media that are described by the fractal Sierpinski carpet.

The aim of this study is to develop a unified model for the permeability, electrical conductivity, and streaming potential coupling coefficient in fractured media by extending the work proposed by Thanh et al. (2021) to partially saturated conditions. For this purpose, we conceptualize a fractured medium as a partially saturated bundle of parallel capillary slits following the fractal scaling law. This conceptualization allows us to determine the capillary pressure-saturation relationship and later deduce expressions for the electrical conductivity and permeability of fractured media under partially saturated conditions. From the electrokinetic streaming current and conduction current within a single slit, we obtain an upscaled expression for the streaming potential coupling coefficient. The new obtained model explicitly depends on properties of fracture water, interface properties, microstructural parameters of fractured media and water saturation. Model predictions are then compared with experimental data, simulated data as well as another previous model in the literature.

THEORETICAL BACKGROUND OF STREAMING POTENTIAL

The streaming current is caused by electrokinetic coupling, that is the drag of electrical charge by water flow in porous media conceptualized as a bundle of cylindrical capillary tubes or a bundle of capillary slits. This phenomenon is directly related to the presence of an electric double layer (EDL) that exists at the solid-water interface of the tubes or fractures (e.g., Overbeek, 1952; Hunter, 1981). This EDL contains an excess of charge in water to compensate the charge deficit of the capillary inner surface. The EDL is composed of the Stern and diffuse layers. The Stern layer only contains counter-ions, i.e., the ions

with opposite sign to the charged surface. The ions in the Stern layer can be considered as immobile due to strong electrostatic attraction. The diffuse layer contains both the counter-ions and co-ions, i.e., the ions with same sign as the charged surface. The ions in the diffuse layer are free to move but with a net excess of charge (e.g., Hunter, 1981; Jougnot et al., 2020). The interface between the Stern layer and the diffuse layer corresponds to the shear plane or slipping plane that separates the stationary fluid and the moving fluid. The electrical potential at this plane is called the zeta potential ζ (V) that mostly depends on mineral composition of porous media, ionic strength, temperature and pH of water (e.g., Hunter, 1981; Vinogradov et al., 2022b). The generated streaming current is, in turn, balanced out by an electrical conduction current in the opposite direction, leading to a so-called streaming potential. At the steady state condition, the streaming potential coupling cofficient (SPCC) is defined as (e.g., Smoluchowski, 1903; Morgan et al., 1989):

$$C_S = \frac{\Delta V}{\Delta P}, \tag{1}$$

where ΔV (V) and ΔP (Pa) are the measured streaming potential and the imposed pressure difference across a probed medium, respectively. There have been two approaches to determine the SPCC at saturated conditions in the literature. For the first approach, the classical one, the SPCC that is expressed in terms of the zeta potential ζ is given by (e.g., Smoluchowski, 1903)

$$C_S = \frac{\epsilon_r \epsilon_0 \zeta}{\eta \sigma_w}, \tag{2}$$

where ϵ_r (no units) is the relative permittivity, ϵ_0 (F/m) is the dielectric permittivity in vacuum, η (Pa s) is the dynamic viscosity and σ_w (S/m) is the electrical conductivity of water. Eq. (2) is called the Helmholtz-Smoluchoski (HS) equation. Note that the surface electrical conductivity σ_s is not considered in Eq. (2). If σ_s is taken into consideration, Eq. (2) can be replaced by the following equation (e.g., Hunter, 1981; Ishido and Mizutani, 1981)

$$C_S = \frac{\epsilon_r \epsilon_0 \zeta}{\eta(\sigma_w + 2\frac{\Sigma_s}{\Lambda})}, \tag{3}$$

where Σ_s (S) is the specific surface conductance and Λ (m) is a characteristic length scale of porous media (Johnson et al., 1986). For the second approach, the SPCC is expressed in terms of the effective excess charge density $\widehat{Q}_v$ (C/m^3) dragged by water (e.g., Kormiltsev et al., 1998; Revil and Leroy, 2004; Jougnot et al., 2020)

$$C_S = -\frac{k\widehat{Q}_v}{\eta\sigma}, \tag{4}$$

where k (m^2) and σ (S/m) are the permeability and electrical conductivity of fully saturated porous media, respectively.

One can note that Thanh et al. (2021) developed a model for the SPCC using the zeta potential ζ for fully saturated fractured media, whereas Guarracino and Jougnot (2022) proposed a model to predict the $\widehat{Q}_v$, for fully and partially water saturated fractured media, that also permits to determine the SPCC.

THEORETICAL DEVELOPMENT

Description of fractured media

Fractures in geological media exist over a wide range of scales, from microns to thousands of kilometers, and fractal patterns for fractured rocks have been reported in published works (e.g., Okubo and Aki, 1987; Bonnet et al., 2001; Kruhl, 2013). To derive the SPCC in fractured media, we regard the geometrical description reported in the literature for fractured media which are assumed to be made up of the fractures and the surrounding matrix (e.g., Tyler and Wheatcraft, 1990; Miao et al., 2015; Roubinet et al., 2016; Guarracino and Jougnot, 2022). The matrix permeability is usually much smaller than that of the fractures and thus the matrix can be considered as impermeable and no fluid exchange through the fracture walls. Note that, for consideration of fluid transfer from the matrix to the fractures, we refer readers to the work reported by Miao et al. (2019), for example. The representative elementary volume (REV) is assumed to be a cuboid of length of L_o (m) and cross-section area A (m^2) as shown in Fig. 1. We conceptualize the fractures of the REV as a bunch

of parallel tortuous slits of varying aperture a (m) and width w (m) following the fractal scaling law (e.g., Tyler and Wheatcraft, 1990; Miao et al., 2015, 2019):

$$f(w) = D_f w_{\max}^{D_f} w^{-D_f-1},\ w_{\min} \leq w \leq w_{\max}, \tag{5}$$

where D_f (no units) is the fractal dimension that is between 1 and 2 in two-dimensional spaces and it can be determined by a box-counting method (e.g., Miao et al., 2015, 2019), $w_{\min}$ (m) and $w_{\max}$ (m) are the smallest and largest fracture widths in the REV, respectively, representing the lower and upper bounds of the fractal distribution. Therefore, the number of fractures whose widths in the range from w to $w+\mathrm{d}w$ is given by $f(w)\mathrm{d}w$ (e.g., Majumdar and Bhushan, 1990; Miao et al., 2015). The total number of fractures, from $w_{\min}$ to $w_{\max}$, is given by

$$N_t = \int_{w_{\min}}^{w_{\max}} f(w)\mathrm{d}w \approx \left(\frac{w_{\max}}{w_{\min}}\right)^{D_f}. \tag{6}$$

Dividing Eq. (5) by Eq. (6), one is able to obtain the probability density function $f_r(w)$

$$f_r(w) = D_f w_{\min}^{D_f} w^{-D_f-1}. \tag{7}$$

It is shown that the aperture a is normally related to the width w by a linear scaling law (e.g., Torabi and Berg, 2011; Miao et al., 2015):

$$a = \beta w, \tag{8}$$

where β (unitless) is the proportionality coefficient called the fracture aspect ratio.

Hydraulic properties

The porosity of the REV is defined as

$$\begin{aligned}\phi =& \frac{V_p}{V_t} = \frac{\int_{w_{\min}}^{w_{\max}} (aw)(L_\tau) f(w)\mathrm{d}w}{L_o A} = \frac{\beta\tau D_f w_{\max}^{D_f}}{A}\int_{w_{\min}}^{w_{\max}} w^{1-D_f}\mathrm{d}w \\ &= \frac{\beta\tau D_f w_{\max}^2}{A(2-D_f)}(1-\alpha^{2-D_f}),\end{aligned} \tag{9}$$

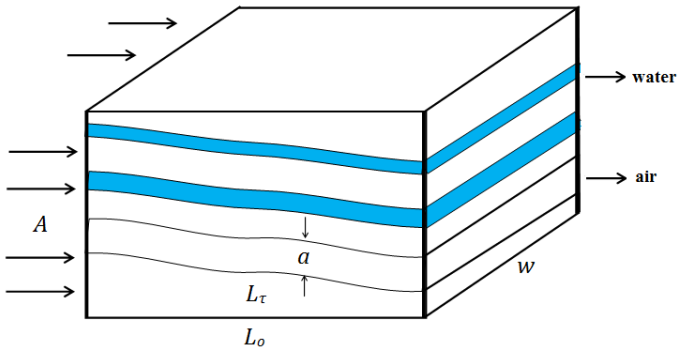

Figure 1: Schematic view of a fractured medium conceptualized as of a bunch of parallel fractures.

where V_p and V_t are the pore volume and total volume of the REV, respectively, L_o is the length of the REV, L_τ is the real length of the fracture, τ=L_τ/L_o is the dimensionless hydraulic tortuosity of the fracture and α=$w_{\min}/w_{\max}$. For the purpose of simplification, the fracture length is assumed to be unchanging with its width, hence τ is considered to be constant over the REV and therefore independent from the water saturation.

We suppose that the REV is initially filled by water and dewatered by the application of a pressure head h (m). For a capillary slit, the relationship between the fracture width w_h and the pressure head h is approximately given by (e.g., Bullard and Garboczi, 2009)

$$h = \frac{2T_s cos\theta}{\rho_w g \beta w_h}, \tag{10}$$

where T_s (N/m) is the surface tension of water, θ (°) is the contact angle, ρ_w (kg/m^3) is the water density and g (m/s^2) is the gravitational acceleration. A fracture is fully desaturated when its width w is greater than value w_h given by Eq. (10). We assume that each fracture is filled by either water or air. Therefore, in water-wet systems, water fills the fractures of the smallest widths, while air occupies fractures of the largest widths when all the fractures are simultaneously accessible. In other words, fractures with widths w comprised between $w_{\min}$ and w_h will be occupied by water while those with widths comprised between w_h and $w_{\max}$ will be filled by air under application of the pressure head h. The contribution of

water in the REV depends on the effective water saturation S_e (unitless), that is defined as

$$S_e = \frac{S_w - S_{wr}}{1 - S_{wr}}, \tag{11}$$

where S_w (unitless) is the water saturation and S_{wr} (unitless) is the residual water saturation that represents the water held as films on the fracture walls which can not be drained by the pressure head h or in non-connected fractures which cannot be taken into account in the present conceptual model.

Following a similar approach to what is reported in the literature (e.g., Guarracino, 2006; Thanh et al., 2020; Guarracino and Jougnot, 2022), S_e is expressed in terms of w_h as follows:

$$S_e = \frac{\int_{w_{\min}}^{w_h} (aw) L_\tau f(w) \mathrm{d}w}{\int_{w_{\min}}^{w_{\max}} (aw) L_\tau f(w) \mathrm{d}w} = \frac{w_h^{2-D_f} - w_{\min}^{2-D_f}}{w_{\max}^{2-D_f} - w_{\min}^{2-D_f}}. \tag{12}$$

Combining Eq. (10) and Eq. (12), the capillary pressure curve for fractured media can be obtained as

$$S_e = \frac{h^{D_f-2} - h_{\max}^{D_f-2}}{h_{\min}^{D_f-2} - h_{\max}^{D_f-2}}, \ h_{\min} \leq h \leq h_{\max}, \tag{13}$$

where $h_{\min} = \frac{2T_s cos\theta}{\rho_w g \beta w_{\max}}$ and $h_{\max} = \frac{2T_s cos\theta}{\rho_w g \beta w_{\min}}$.

Under laminar flow conditions, the average velocity in a single fracture of aperture a is given by (e.g., Chung, 2010)

$$\overline{v} = \frac{\rho_w g a^2}{12\eta\tau} \frac{\Delta h}{L_o}, \tag{14}$$

where Δh is the pressure head drop across the REV.

The flow rate in a single fracture follows the well-known cubic law as (e.g., Neuzil and Tracy, 1981; Klimczak et al., 2010)

$$q = \overline{v}.(aw) = \frac{\rho_w g a^3 w}{12\eta\tau} \frac{\Delta h}{L_o}. \tag{15}$$

The total volumetric flow through the REV under unsaturated conditions is given by

$$q^{\mathrm{REV}} = \int_{w_{\min}}^{w_h} q f(w) \mathrm{d}w. \tag{16}$$

Combining Eq. (5), Eq. (8), Eq. (15) and Eq. (16), one obtains

$$\begin{aligned} q^{\mathrm{REV}} &= \int_{w_{\min}}^{w_h} \frac{\rho_w g a^3 w}{12\eta\tau} \frac{\Delta h}{L_o} [D_f w_{\max}^{D_f} w^{-D_f-1} \mathrm{d}w] \\ &= \frac{\rho_w g \beta^3 D_f}{12\eta\tau} w_{\max}^{D_f} \frac{w_h^{4-D_f} - w_{\min}^{4-D_f}}{4-D_f} \frac{\Delta h}{L_o}. \end{aligned} \tag{17}$$

Combining Eq. (12) and Eq. (17), one can express q^{REV} in terms of S_e as

$$q^{\mathrm{REV}} = \frac{\rho_w g \beta^3 D_f}{12\eta\tau} w_{\max}^4 \frac{\left[S_e(1-\alpha^{2-D_f}) + \alpha^{2-D_f}\right]^{\frac{4-D_f}{2-D_f}} - \alpha^{4-D_f}}{4-D_f} \frac{\Delta h}{L_o}. \tag{18}$$

Following Darcy′s law for Newtonian fluid flow in fractured media, q^{REV} is given by

$$q^{\mathrm{REV}} = \frac{kA}{\eta} \frac{\rho_w g \Delta h}{L_o}, \tag{19}$$

where k and A are the permeability and the cross sectional area of the REV.

Combining Eq. (18) and Eq. (19), we obtain an expression for k under unsaturated conditions as

$$k(S_e) = \frac{\beta^3 D_f}{12\tau A} w_{\max}^4 \frac{\left[S_e(1-\alpha^{2-D_f}) + \alpha^{2-D_f}\right]^{\frac{4-D_f}{2-D_f}} - \alpha^{4-D_f}}{4-D_f}. \tag{20}$$

Hence, the permeability under fully saturated conditions ($S_e = 1$) is given by

$$k_s = \frac{\beta^3 D_f}{12\tau A} w_{\max}^4 \frac{1-\alpha^{4-D_f}}{4-D_f}. \tag{21}$$

The relative permeability of fractured media, that is defined as $k_r = k(S_e)/k_s$, is given by

$$k_r(S_e) = \frac{\left[S_e(1-\alpha^{2-D_f}) + \alpha^{2-D_f}\right]^{\frac{4-D_f}{2-D_f}} - \alpha^{4-D_f}}{1-\alpha^{4-D_f}}. \tag{22}$$

It is remarked that using a classical fractal object known as the Sierpinski carpet for the fracture network in combination with the Burdine model, Guarracino (2006) obtained an expression for k_r as a function of S_e as follows:

$$k_r(S_e) = S_e^2 \frac{\left[S_e(1-\alpha^{2-D_f}) + \alpha^{2-D_f}\right]^{\frac{4-D_f}{2-D_f}} - \alpha^{4-D_f}}{1-\alpha^{4-D_f}}. \tag{23}$$

The only difference between our proposed model given by Eq. (22) and the one proposed by Guarracino (2006) given by Eq. (23) for k_r is a prefactor S_e^2.

If one invokes Eq. (9), k_s can be expressed as

$$k_s = \frac{\beta^2 w_{\max}^2 \phi}{12\tau^2} \frac{1-\alpha^{4-D_f}}{1-\alpha^{2-D_f}} \frac{2-D_f}{4-D_f} = \frac{a_{\max}^2 \phi}{12\tau^2} \frac{1-\alpha^{4-D_f}}{1-\alpha^{2-D_f}} \frac{2-D_f}{4-D_f}. \tag{24}$$

For $w_{max} >> w_{min}$ ($\alpha \to 0$) that is normally reported to be satisfied for the fractal fractured media (e.g., Guarracino, 2006; Miao et al., 2015, 2019; Thanh et al., 2021), Eq. (24) reduces to

$$k_s = \frac{\beta^2 w_{\max}^2 \phi}{12\tau^2} \frac{2-D_f}{4-D_f} = \frac{a_{\max}^2 \phi}{12\tau^2} \frac{2-D_f}{4-D_f}. \tag{25}$$

Electrical conductivity

Following Thanh et al. (2021), the total electrical conductivity in a single fracture with consideration of the surface conductivity is given by

$$\sigma_f(w) = \sigma_w \frac{\beta w^2}{A\tau} + \Sigma_s \frac{2(1+\beta)w}{A\tau}. \tag{26}$$

Recall that σ_w (S/m) and Σ_s (S) are the electrical conductivity of water and specific surface conductance at the solid–water interface as previously mentioned.

The total electrical conductivity of considered porous media under unsaturated conditions is therefore obtained by

$$\sigma = \int_{w_{\min}}^{w_h} \sigma_f(w) f(w) \mathrm{d}w. \tag{27}$$

Combining Eq. (5), Eq. (26) and Eq. (27) yields the following:

$$\begin{aligned}\sigma =& \frac{1}{A\tau}\left\{\sigma_w \beta D_f w_{\max}^{D_f} \frac{w_h^{2-D_f} - w_{\min}^{2-D_f}}{2-D_f} + 2\Sigma_s(1+\beta) D_f w_{\max}^{D_f} \frac{w_h^{1-D_f} - w_{\min}^{1-D_f}}{1-D_f}\right\}. \\ =& \frac{\beta D_f w_{\max}^{D_f}(w_h^{2-D_f} - w_{\min}^{2-D_f})}{A(2-D_f)\tau}\left\{\sigma_w + \frac{2(1+\beta)\Sigma_s}{\beta}\frac{2-D_f}{1-D_f}\frac{w_h^{1-D_f} - w_{\min}^{1-D_f}}{w_h^{2-D_f} - w_{\min}^{2-D_f}}\right\}.\end{aligned} \tag{28}$$

Invoking Eq. (12), the σ under unsaturated conditions is expressed in terms of S_e as

$$\sigma = \frac{\beta D_f w_{\max}^2 S_e(1-\alpha^{2-D_f})}{A(2-D_f)\tau}\left\{\sigma_w + \frac{2(1+\beta)\Sigma_s}{\beta w_{\max}}\frac{2-D_f}{1-D_f}\frac{\left[S_e(1-\alpha^{2-D_f}) + \alpha^{2-D_f}\right]^{\frac{1-D_f}{2-D_f}} - \alpha^{1-D_f}}{S_e(1-\alpha^{2-D_f})}\right\}. \tag{29}$$

Substituting A from Eq. (9) into Eq. (28), the σ is obtained as

$$\sigma = \frac{\phi S_e}{\tau^2}\left\{\sigma_w + \frac{2(1+\beta)\Sigma_s}{\beta w_{\max}}\frac{2-D_f}{1-D_f}\frac{\left[S_e(1-\alpha^{2-D_f}) + \alpha^{2-D_f}\right]^{\frac{1-D_f}{2-D_f}} - \alpha^{1-D_f}}{S_e(1-\alpha^{2-D_f})}\right\}. \tag{30}$$

Eq. (30) shows the dependence of σ under unsaturated conditions on microstructural parameters of the fractured media (D_f, ϕ, α, β, w_{max}, τ), water electrical conductivity σ_w, specific surface conductance Σ_s, and effective water saturation S_e.

Streaming potential coupling coefficient

Streaming current through the REV

Under the thin EDL assumption in which the Debye length is small compared to fracture widths and the Debye-Hückel approximation that is applicable for small values of ζ (i.e., 50 mV) for a binary symmetric 1:1 electrolyte, for example (e.g., Rice and Whitehead, 1965; Pride, 1994), the electrokinetic streaming current in a single fracture due to transport of excess charge in the EDL by water flow is given by (e.g., Thanh et al., 2021)

$$i_s(w) = -\frac{\epsilon_r \epsilon_o \zeta}{\eta}\frac{wa}{\tau}\frac{\rho_w g \Delta h}{L_o} = -\frac{\epsilon_r \epsilon_o \zeta}{\eta}\frac{\beta w^2}{\tau}\frac{\rho_w g \Delta h}{L_o}. \tag{31}$$

The total streaming current through the REV under unsaturated conditions is determined by

$$I_s = \int_{w_{\min}}^{w_h} i_s(w) f(w) \mathrm{d}w \tag{32}$$

From Eq. (5), Eq. (31) and Eq. (32), the following is obtained

$$\begin{aligned} I_s =& -\frac{\epsilon_r \epsilon_o \zeta}{\eta \tau} \frac{\rho_w g \Delta h}{L_o} (\beta D_f w_{\max}^{D_f}) \int_{w_{\min}}^{w_h} w^{1-D_f} \mathrm{d}w \\ =& -\frac{\epsilon_r \epsilon_o \zeta \beta D_f}{\eta \tau} \frac{w_{\max}^{D_f}}{(2-D_f)} (w_h^{2-D_f} - w_{\min}^{2-D_f}) \frac{\rho_w g \Delta h}{L_o}. \end{aligned} \tag{33}$$

Conduction current through the REV

The streaming current is accounted for the streaming potential ΔV that is built up across the REV due to the water flow. In turn, an electric conduction current is generated in the REV due to the electrical potential difference ΔV. Namely, the conduction current in a single fracture is given by Thanh et al. (2021)

$$i_c(w) = \left[\sigma_w \frac{\beta w^2}{L_o \tau} + \Sigma_s \frac{2(1+\beta) w}{L_o \tau} \right] \Delta V. \tag{34}$$

The total electric conduction current through the REV under unsaturated conditions is given by

$$\begin{aligned} I_c =& \int_{w_{\min}}^{w_h} i_c(w) f(w) \mathrm{d}w \\ =& \frac{\beta D_f w_{\max}^{D_f} (w_h^{2-D_f} - w_{\min}^{2-D_f})}{(2-D_f)\tau} \left[\sigma_w + \frac{2(1+\beta)\Sigma_s}{\beta} \frac{2-D_f}{1-D_f} \frac{w_h^{1-D_f} - w_{\min}^{1-D_f}}{w_h^{2-D_f} - w_{\min}^{2-D_f}} \right] \frac{\Delta V}{L_o}. \end{aligned} \tag{35}$$

Streaming potential coupling coefficient

Considering thermodynamic equilibrium, the following condition is satisfied

$$I_s + I_c = 0. \tag{36}$$

Consequently, the SPCC is given by

$$C_S = \frac{\Delta V}{\Delta P} = \frac{\Delta V}{\rho_w g \Delta h} = \frac{\epsilon_r \epsilon_0 \zeta}{\eta \left[\sigma_w + \frac{2(1+\beta)\Sigma_s}{\beta} \frac{2-D_f}{1-D_f} \frac{w_h^{1-D_f} - w_{\min}^{1-D_f}}{w_h^{2-D_f} - w_{\min}^{2-D_f}} \right]}. \tag{37}$$

Invoking Eq. (12), the SPCC can be expressed in terms of S_e as

$$C_S = \frac{\epsilon_r \epsilon_0 \zeta}{\eta \left[\sigma_w + \frac{2(1+\beta)\Sigma_s}{\beta w_{\max}} \frac{2-D_f}{1-D_f} \frac{\left[S_e(1-\alpha^{2-D_f}) + \alpha^{2-D_f} \right]^{\frac{1-D_f}{2-D_f}} - \alpha^{1-D_f}}{S_e(1-\alpha^{2-D_f})} \right]}. \tag{38}$$

Eq. (38) is an expression for the SPCC of fractured media under unsaturated conditions. It predicts that the SPCC is dependent of water properties (σ_w, ϵ_r and η), physico-chemical properties of the solid–water interface (Σ_s and ζ), microstructural parameters of fractured media (D_f, ϕ, α, β, $w_{\max}$) and saturation state (S_e). When $\Sigma_s = 0$, Eq. (38) reduces to the HS equation given by Eq. (2) that has been proposed for porous media rather than fractured media regardless of S_e. Under saturated conditions $S_e = 1$, Eq. (38) simplifies to that proposed by Thanh et al. (2021):

$$C_S = \frac{\epsilon_r \epsilon_0 \zeta}{\eta \left[\sigma_w + \frac{2(1+\beta)\Sigma_s}{\beta w_{\max}} \frac{2-D_f}{1-D_f} \frac{1-\alpha^{1-D_f}}{1-\alpha^{2-D_f}} \right]}. \tag{39}$$

Combining Eq. (4), Eq. (30) and Eq. (38), one can infer an expression for the effective excess charge density as following

$$\widehat{Q}_v = -\epsilon_r \epsilon_0 \zeta \frac{\phi S_e}{k \tau^2}. \tag{40}$$

We remark that Guarracino and Jougnot (2022) proposed a model for $\widehat{Q}_v$, that is deduced from their Eq. (14) and Eq. (23), as below

$$\widehat{Q}_v = -\epsilon_r \epsilon_0 \zeta \left[1 + \frac{1}{54} \left(\frac{e\zeta}{k_B T} \right)^2 \right] \frac{\phi S_e}{k}, \tag{41}$$

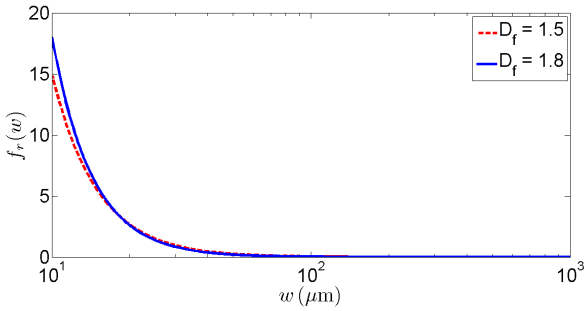

Figure 2: Probability density function associated with fracture size distribution in this work in the width range from $w_{\min} = 10$ μm to $w_{\max} = 1000$ μm ($\alpha = 0.01$) for two values of D_f (1.5 and 1.8).

where e (C) the elementary charge, k_B (J/K) the Boltzman constant and T (K) is the absolute temperature.

Under the Debye-Hückel approximation in which $\left(\frac{e\zeta}{2k_BT}\right)^2 << 1$ (e.g., Pride, 1994), Eq. (41) reduces to

$$\widehat{Q}_v = -\epsilon_r \epsilon_0 \zeta \frac{\phi S_e}{k}. \tag{42}$$

Obviously, our finding given by Eq. (40) is the same as that proposed by Guarracino and Jougnot (2022) under the Debye-Hückel approximation given by Eq. (42). It is noted that Guarracino and Jougnot (2022) did not consider τ in their model (i.e., $\tau = 1$).

RESULTS AND DISCUSSION

Sensitivity of the model

Figure 2 shows the representative probability density function of fractures predicted from Eq. (7) in the width range from $w_{\min} = 10$ μm to $w_{\max} = 1000$ μm ($\alpha = 0.01$) for two different values of D_f (1.5 and 1.8). It is seen that: (i) the frequency distribution of fractures becomes skewed toward smaller fracture width and (ii) there is a larger number of small fractures for larger value of D_f.

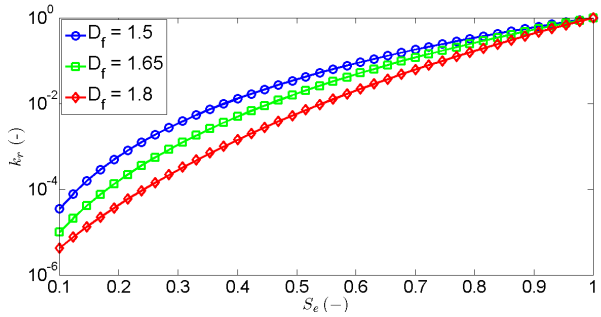

(a)

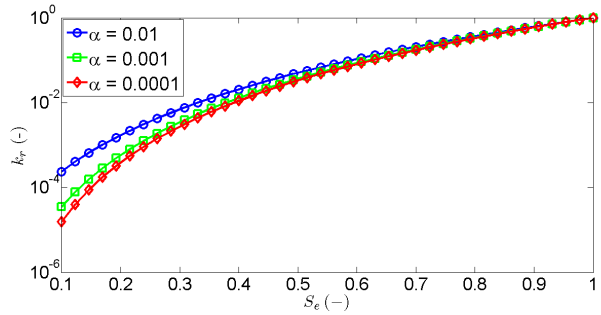

(b)

Figure 3: Variation of the k_r with S_e predicted from Eq. (22): (a) for three representative values of D_f (1.5, 1.65 and 1.8) at a given representative value of α=0.001, (b) for three representative values of α (0.01, 0.001 and 0.0001) at a given representative value of D_f = 1.5.

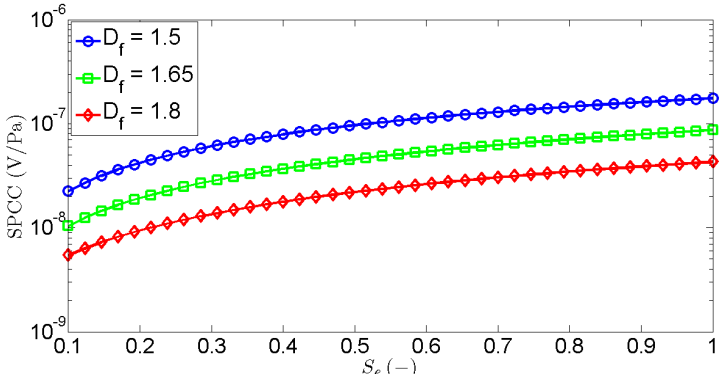

Figure 4: Dependence of the SPCC in magnitude on the effective water saturation for different values of D_f (1.6, 1.65 and 1.8) predicted from Eq. (38)

From Eq. (22), we can predict the variation of k_r with S_e for fractured media. For example, Fig. 3 shows the S_e-k_r relationship for: (a) three representative values of D_f (1.5, 1.65 and 1.8) at a given representative value of α=0.001, (b) three representative values of α (0.01, 0.001 and 0.0001) at a given representative value of $D_f = 1.5$. It is seen that k_r is sensitive to parameters of S_e, D_f and α. At given values of S_e and α, k_r decreases with an increase of D_f. The reason is that when D_f increases, the number of fractures in the REV with small widths increases as indicated in Fig. 2. Therefore, at the same water saturation, w_h decreases and the total flow rate through the REV becomes smaller. Consequently, k_r decreases with increasing D_f. It is also predicted that at given values of S_e and D_f, k_r decreases with a decrease of α. The reason is that when α decreases, there is a larger fraction of fractures with smaller widths due to the property of the fractal distribution. As a result, k_r decreases.

Figure 4 shows the variation of the SPCC in magnitude with S_e for different values of D_f (1.6, 1.65 and 1.8) predicted from Eq. (38). Representative parameters used in Eq. (38) are: $\sigma_w = 0.02$ S/m, $\Sigma_s = 10^{-9}$ S, ζ = -0.030 V, $w_{\max} = 200.10^{-6}$ m and $\beta = 0.01$. It is shown that the SPCC in magnitude increases with increasing S_e. This prediction is in good agreement with those observed in published work but for porous media such as sand columns, dolomite cores or limestone cores (e.g., Guichet et al., 2003; Revil and Cerepi,

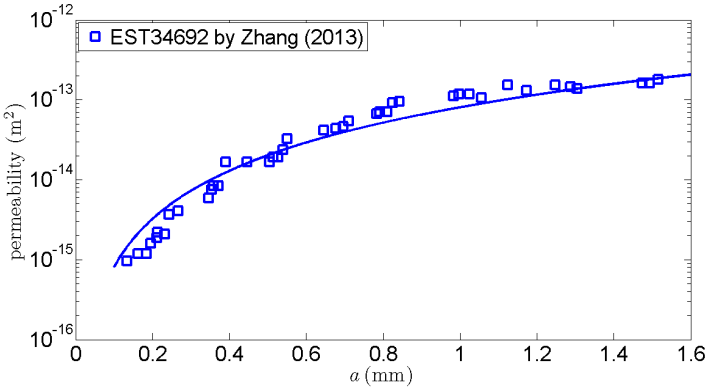

Figure 5: Variation of the k_s of a single fracture as a function of aperture a obtained from Zhang (2013) for the sample EST34692 and prediction from Eq. (25) for a fractured medium with $D_f = 1.8$, $\tau = 1.2$, $\phi = 0.025$ and $a_{\max} = a/40$.

2004; Vinogradov and Jackson, 2011). Additionally, it is also seen that the SPCC decreases with increasing D_f for the same value of S_e. The reason is that when D_f increases, the number of fractures characterized by relatively small widths increases as shown by Fig. 2. Hence, the surface conductivity of fractured media increases and the SPCC in magnitude decreases. It is remarked that the surface conductivity of fractured media is dominated by the contribution from the smaller width fractures for given values of σ_w and Σ_s.

Comparison with published data

There are not many published experimental data of single fracture permeability measurement in the literature. Nevertheless, Zhang (2013) presents gas permeability measurement on a Callovo-Oxfordian (COx) clayrock sample which exhibits a single fracture. Non fractured COx clay rocks are known for their very low permeability (typically 10 nd at saturation as indicated by Jougnot et al. (2010)). Hence, the measured permeability of a fractured sample is largely due to the fracture itself. Fig. 5 shows the evolution of the sample permeability as a function of the aperture a of the fracture. The variation of the fractured medium k_s under saturated conditions with $a_{\max}$ is predicted from Eq. (25) as shown by the solid line in Fig. 5. The model can describe the behavior of the permeability well with

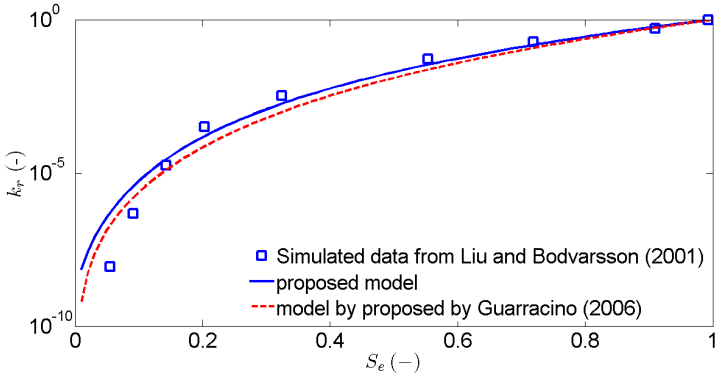

Figure 6: Variation of k_r with S_e simulated by Liu and Bodvarsson (2001) for two dimensional fracture networks (symbols) and corresponding predictions from Eq. (22) and Eq. (23.

$D_f = 1.8$, $\tau = 1.2$, $\phi = 0.025$, $a_{\max} = a/40$. It should be remarked that the fitting parameters (D_f, τ, ϕ) are optimized using a function "fmincon" in Matlab to seek a minimum root-mean-square error between the experimental data and predicted values.

Figure 6 shows the variation of k_r with S_e simulated by Liu and Bodvarsson (2001) for two dimensional fracture networks (symbols). This observation can be predicted by Eq. (22) with optimized parameters $D_f = 1.6$ and $\alpha = 2.5\times10^{-4}$ (solid line). As pointed out by Guarracino (2006), the simulated data in Fig. 6 can also be reproduced by Eq. (23) with $D_f = 1.5$ and $\alpha = 0.01$ (dashed line). It is seen that the proposed model is in very good agreement with simulated data and the model proposed by Guarracino (2006) (The root mean square deviation (RMSD) of the proposed model and that of Guarracino (2006) are calculated to be 0.0241 and 0.0254, respectively).

Similarly, Fig. 7 shows the variation of k_r with S_e for the fractured wellbore cement measured by Rod et al. (2019) (symbols) and corresponding predictions from our model and Guarracino (2006). The fitting parameters are optimized in the same way as previously mentioned are $D_f = 1.2$, $\alpha = 0.001$ and $D_f = 1.1$, $\alpha = 0.01$ for Eq. (22) and Eq. (23), respectively. One can see that our proposed model (RMSD = 0.0985) can provide a better fit than Guarracino (2006) (RMSD = 0.1469). The main reason may be come from the

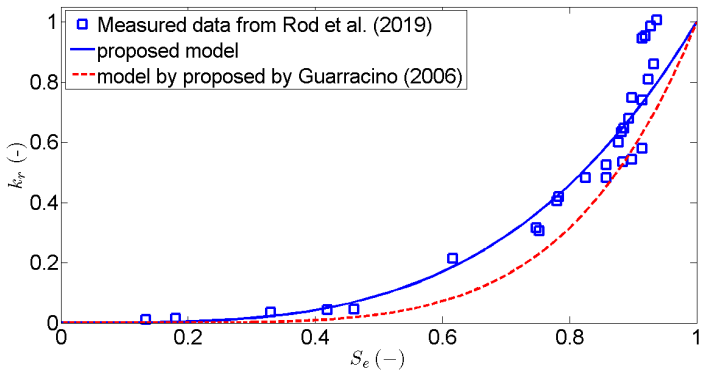

Figure 7: Variation of k_r with S_e for the fractured welbore cement measured by Rod et al. (2019) (symbols) and corresponding predictions from Eq. (22) and Eq. (23.

difference in the prefactor S_e^2 in Eq. (23) compared to Eq. (22). Therefore, k_r predicted from Guarracino (2006) is lower than our model, especially at low values of S_e. Note that S_e is always less than 1.

To the best of our knowledge, there have been only few publications on SPCC measurements of fractured media under saturated conditions (e.g., Moore and Glaser, 2007; Vinogradov et al., 2022a) and no publications under unsaturated conditions. For example, Fagerlund and Heinson (2003) measured the zeta potential of fractured rocks by crushing rocks and packing obtained crushed material into a tube. Hence, the experimental data for crushed material reported by Fagerlund and Heinson (2003) is not applicable for our model. Vinogradov et al. (2022a) measured the SPCC for a fractured Lewisian gneiss sample which was assumed to have a single fracture at different values of confining pressure and ionic strengths. For example, the measured values for the SPCC at two different values of confining pressures (4 MPa and 7 MPa) for the ionic strength of NaCl of 0.7 M, that is denoted by C_f were reported to be -1.21 mV/MPa and -1.23 mV/MPa, respectively. The pore electrical conductivity σ_w can be estimated by the relationship $\sigma_w = 10C_f = 7$ S/m (e.g., Sen and Goode, 1992). For this high value of σ_w, the contribution of the surface conductivity to the total effective conductivity can be neglected (e.g., Alkafeef and Alajmi, 2006; Thanh

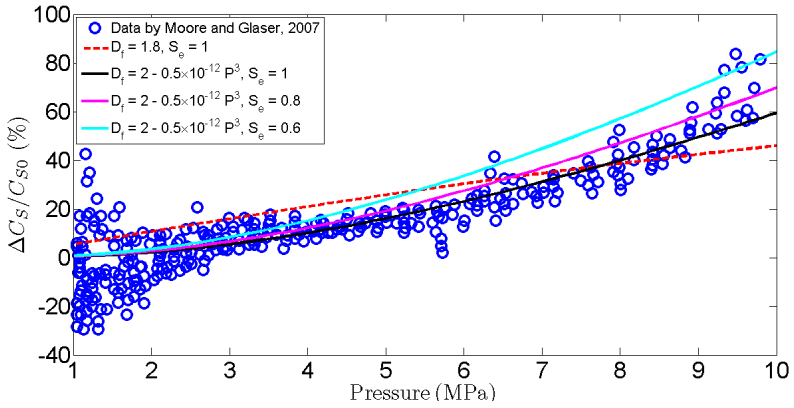

Figure 8: Variation of the relative SPCC difference with injection pressure $\Delta C_S(P)/C_{S0}$. The symbols are experimental data reported by Moore and Glaser (2007). The best fit of the proposed model to experimental data are displayed by lines.

and Sprik, 2016). Therefore, we can apply Eq.(39) without consideration of the term of $\frac{2(1+\beta)\Sigma_s}{\beta w_{\max}} \frac{2-D_f}{1-D_f} \frac{1-\alpha^{1-D_f}}{1-\alpha^{2-D_f}}$ to determine the ζ. The obtained values of the ζ are -11.8 mV and -12.0 mV for the confining pressures of 4 MPa and 7 MPa, respectively. This finding is in good agreement with the result of Vinogradov et al. (2022a) where ζ was reported to be -10.52 mV and -10.69 mV, respectively.

Additionally, Moore and Glaser (2007) measured the relative SPCC difference as a function of injection pressures for microcracked Sierra granite samples during hydraulic fracturing in the laboratory as shown in Fig. 8 (symbols). It is remarked that the relative SPCC difference is defined as $\Delta C_S(P)/C_{S0}$, where C_{S0} is the SPCC at zero pressure drop. It is seen that there is a tendency of increase of the SPCC with pressure. The reason is related to an increase of dilatancy of microcracks with increasing pressures, which causes an increase in permeability and therefore in apertures. The increase of apertures of fractured media results in a decrease of the surface electrical conductivity and hence the SPCC. Moore and Glaser (2007) showed the variation of the permeability k_s with pressure drop P as follows:

$$k_s = 10^{-18} e^{2.5\times10^{-4}P}, \tag{43}$$

where k_s is in m^2 and P is in kPa.

Combining Eq. (24) and Eq. (43), one can obtain $w_{\max}$ as a function of P as following:

$$w_{\max} = \chi\sqrt{k_s} = \chi 10^{-9} e^{1.25\times10^{-4}P}, \tag{44}$$

where $\chi = \frac{\tau}{\beta}\sqrt{\frac{12(1-\alpha^{2-D_f})(4-D_f)}{\phi(1-\alpha^{4-D_f})(2-D_f)}}$.

From Eq. (39) and Eq. (44), one can predict the $\Delta C_S/C_{S0}$ as a function of P for the microcracked samples reported by Moore and Glaser (2007) as shown by the solid line in Fig. 8. Input parameters for the prediction are shown in Table 1 where superscripts * stands for values measured by Moore and Glaser (2007) and superscripts $^+$ stands for fitting parameters. Namely, σ_w, ϕ, and ζ are reported to be 0.015 S/m, 0.009 (unitless) and -34 mV, respectively. Due to constraints associated with a large number of model parameters for $\Delta C_S/C_{S0}$, we search for those parameters that provide a relatively good fit by a trial-and-error method. The obtained values for τ, Σ_s, D_f, β, and α are 2 (unitless), 0.17×10^{-10} S, 1.8 (unitless), 0.01 (unitless), and 0.001 (unitless), respectively. it is noted that the found fitting parameters are in the ranges normally reported in literature for fractured rocks. For example, τ was reported between 1.1 and 30 (e.g., Wang et al., 2022; Violay et al., 2010; Roubinet et al., 2018). Using the box-counting technique, D_f was found between 1.2 and 1.85 (e.g., Walsh and Watterson, 1993; Roy et al., 2007). The surface conductance Σ_s was reported in the range from 0.1×10^{-9} S to 4×10^{-9} S for silica surface in contact with NaCl electrolytes (e.g., Thanh et al., 2019; Revil and Glover, 1998). Ghanbarian et al. (2019) found β in the range from 0.001 to 0.1 for tensile fractures in the Krafla fissure swarm of northeast Iceland. Additionally, Miao et al. (2015) also used $\beta = 0.002$ for fitting their model with simulated data. Values of α were inferred between 0.0001 and 0.01 for fractured carbonate core rock samples (e.g., Erol et al., 2017). Fig. 8 shows that the proposed model can produce the key behavior of experimental data. We remark that the model can provide a better fit if one takes into account the variation of D_f with P (Guarracino and Jougnot, 2022). For example, the relationship $D(P) = 2 - 0.5\times10^{-12}P^3$ provides a better fit to the experimental data as shown in Fig. 8. We also illustrate variations of $\Delta C_S/C_{S0}$ with P

Table 1: Input parameters for the microcracked samples reported by Moore and Glaser (2007). Note that superscripts * stands for values measured by Moore and Glaser (2007) and superscripts $^+$ stands for fitting parameters

Parameter	**Value**	**Units**
σ_w^*	0.015	S/m
ϕ^*	0.009	unitless
τ^+	2	unitless
ζ^*	-34	mV
Σ_s^+	0.17×10^{-10}	S
D_f^+	1.8	unitless
β^+	0.01	unitless
α^+	0.001	unitless

predicted from the proposed model for other effective saturations S_e (0.8 and 0.6) as shown by the colored solid lines in Fig. 8.

CONCLUSIONS

We present a new unified model for the permeability, electrical conductivity, and streaming potential coupling coefficient in variably saturated fractured media. For those, we conceptualize the fractured medium as a bundle of parallel capillary fractures or slits with varying sizes that is partially saturated. We assume that the fracture size distribution of the corresponding medium follows the fractal scaling law, therefore allowing us to determine the pressure head-water saturation relationship. From the flow rate, conduction current, and electrokinetic streaming current within a single saturated fracture, we can upscale expressions for the permeability, relative permeability, electrical conductivity, and streaming potential coupling coefficient for fractured media under partially saturated conditions at the REV scale. This new unified model explicitly depends on properties of fracture water (σ_w, ϵ_r and η), interface properties (Σ_s and ζ), microstructural parameters of fractured media (D_f, ϕ, α, β, $w_{\max}$) and saturation state (S_e). Model predictions are in good with experimental data, simulated data as well as another previous model in the literature. This newly proposed model constitutes a practical framework to estimate hydraulic properties and monitor water flow in fractured media based on self potential measurements and pos-

sibly monitor fracking processes.

DATA AVAILABILITY STATEMENT

The data underlying this article will be shared on reasonable request to the corresponding author.

REFERENCES

Aizawa, K., Y. Ogawa, and T. Ishido, 2009, Groundwater flow and hydrothermal systems within volcanic edifices: Delineation by electric self-potential and magnetotellurics: Journal of Geophysical Research, **114**.

Alkafeef, S. F., and A. F. Alajmi, 2006, Streaming potentials and conductivities of reservoir rock cores in aqueous and non-aqueous liquids: Colloids and Surfaces A: Physicochem. Eng. Aspects, **289**, 141–148.

Binley, A., S. S. Hubbard, J. A. Huisman, A. Revil, D. A. Robinson, K. Singha, and L. D. Slater, 2015, The emergence of hydrogeophysics for improved understanding of subsurface processes over multiple scales: Water Resources Research, **51**, 3837–3866.

Bodvarsson, G., W. Boyle, R. Patterson, and D. Williams, 1999, Overview of scientific investigations at yucca mountain—the potential repository for high-level nuclear waste: Journal of Contaminant Hydrology, **38**, 3–24.

Bonnet, E., O. Bour, N. E. Odling, P. Davy, I. Main, P. Cowie, and B. Berkowitz, 2001, Scaling of fracture systems in geological media: Reviews of Geophysics, **39**, 347–383.

Bullard, J. W., and E. J. Garboczi, 2009, Capillary rise between planar surfaces: Phys. Rev. E, **79**, no. 1, 011604.

Chung, C., 2010, Extrusion of polymers 2e: Theory and practice: Hanser Publications; 2nd edition.

Clair, J. S., S. Moon, W. S. Holbrook, J. T. Perron, C. S. Riebe, S. J. Martel, B. J. Carr, C. Harman, K. Singha, and D. D. Richter, 2015, Geophysical imaging reveals topographic stress control of bedrock weathering: Science, **350**, 534 – 538.

Corwin, R. F., and D. B. Hoover, 1979, The self-potential method in geothermal exploration: Geophysics, **44**, 226–245.

Demirel, S., D. Roubinet, J. Irving, and E. Voytek, 2018, Characterizing near-surface fractured-rock aquifers: Insights provided by the numerical analysis of electrical resistivity experiments: Water, **10**, 1117.

DesRoches, A. J., K. E. Butler, and K. T. MacQuarrie, 2018, Surface self-potential patterns related to transmissive fracture trends during a water injection test: Geophysical Journal

International, **212**, 2047–2060.

Doussan, C., L. Jouniaux, and J.-L. Thony, 2002, Variations of self-potential and unsaturated water flow with time in sandy loam and clay loam soils: Journal of Hydrology, **267**, 173 – 185.

Erol, S., S. Fowler, V. Harcouët-Menou, and B. Laenen, 2017, An analytical model of porosity - permeability for porous and fractured media: Transport in Porous Media, **120**, 327–358.

Fagerlund, F., and G. Heinson, 2003, Detecting sub-surface groundwater flow in fractured rock using self- potential (sp) methods: Environmental Geology, **43**, 782–794.

Finizola, A., N. Lenat, O. Macedo, D. Ramos, J. Thouret, and F. Sortino, 2004, Fluid circulation and structural discontinuities inside misti volcano (peru) inferred from sel-potential measurements: Journal of Volcanology and Geothermal Research, **135**, 343–360.

Ghanbarian, B., E. Perfect, and H.-H. Liu, 2019, A geometrical aperture-width relationship for rock fractures: Fractals, **27**, 1940002.

Grobbe, N., and S. Barde-Cabusson, 2019, Self-potential studies in volcanic environments: A cheap and efficient method for multiscale fluid-flow investigations: International Journal of Geophysics, **2019**, 1–19.

Guarracino, L., 2006, A fractal constitutive model for unsaturated flow in fractured hard rocks: Journal of Hydrology, **324**, 154–162.

Guarracino, L., and D. Jougnot, 2022, A fractal model for effective excess charge density in variably saturated fractured rocks: Journal of Geophysical Research: Solid Earth, **127**, e2021JB022982.

Guichet, X., L. Jouniaux, and J.-P. Pozzi, 2003, Streaming potential of a sand column in partial saturation conditions: Journal of Geophysical Research: Solid Earth, **108**.

Haas, A. K., A. Revil, M. Karaoulis, L. Frash, J. Hampton, M. Gutierrez, and M. Mooney, 2013, Electric potential source localization reveals a borehole leak during hydraulic fracturing: GEOPHYSICS, **78**, D93–D113.

Herwanger, J., M. Worthington, R. Lubbe, A. Binley, and J. Khazanehdari, 2004, A comparison of cross-hole electrical and seismic data in fractured rock: Geophysical Prospecting,

52, 109–121.

Hu, K., D. Jougnot, Q. Huang, M. C. Looms, and N. Linde, 2020, Advancing quantitative understanding of self-potential signatures in the critical zone through long-term monitoring: Journal of Hydrology, **585**, 124771.

Hunter, R. J., 1981, Zeta potential in colloid science: Academic, New York.

Ishido, T., and H. Mizutani, 1981, Experimental and theoretical basis of electrokinetic phenomena in rock-water systems and its applications to geophysics: Journal of Geophysical Research, **86**, 1763–1775.

Jardani, A., A. Revil, A. Boleve, A. Crespy, J.-P. Dupont, W. Barrash, and B. Malama, 2007, Tomography of the darcy velocity from self-potential measurements: Geophysical Research Letters, **34**.

Johnson, D. L., J. Koplik, and L. M. Schwartz, 1986, New pore-size parameter characterizing transport in porous media: Phys. Rev. Lett., **57**, no. 20, 2564–2567.

Jougnot, D., N. Linde, E. Haarder, and M. Looms, 2015, Monitoring of saline tracer movement with vertically distributed self-potential measurements at the hobe agricultural test site, voulund, denmark: Journal of Hydrology, **521**, 314 – 327.

Jougnot, D., A. Revil, N. Lu, and A. Wayllace, 2010, Transport properties of the callovo-oxfordian clay rock under partially saturated conditions: Water Resources Research, **46**.

Jougnot, D., D. Roubinet, L. Guarracino, and A. Maineult, 2020, Modeling streaming potential in porous and fractured media, description and benefits of the effective excess charge density approach: In: Biswas A., Sharma S. (eds) Advances in Modeling and Interpretation in Near Surface Geophysics. Springer Geophysics. Springer, Cham.

Jouniaux, L., J. Pozzi, J. Berthier, and P. Masse', 1999, Detection of fluid flow variations at the nankai trough by electric and magnetic measurements in boreholes or at the seafloor: Journal of Geophysical Research, **104**, 29293–29309.

Klimczak, C., R. Schultz, R. Parashar, and D. Reeves, 2010, Cubic law with aperture-length correlation: Implications for network scale fluid flow: Hydrogeology Journal, **18**, 851–862.

Kormiltsev, V. V., A. N. Ratushnyak, and V. A. Shapiro, 1998, Three-dimensional modeling of electric and magnetic fields induced by the fluid flow movement in porous media: Physics of the Earth and Planetary Interiors, **105**, 109 – 118.

462 Kruhl, J. H., 2013, Fractal-geometry techniques in the quantification of complex rock struc-
463 tures: A special view on scaling regimes, inhomogeneity and anisotropy: Journal of
464 Structural Geology, **46**, 2–21.
465 Li, X.-Y., 1997, Fractured reservoir delineation using multicomponent seismic data: Geo-
466 physical Prospecting, **45**, 39–64.
467 Liu, H.-H., and G. S. Bodvarsson, 2001, Constitutive relations for unsaturated flow in a
468 fracture network: Journal of Hydrology, **252**, 116–125.
469 Maineult, A., B. Thomas, C. Nussbaum, K. Wieczorek, D. Gibert, B. Lavielle, B. Ker-
470 gosien, F. Nicollin, K. Mahiouz, and N. Lesparre, 2013, Anomalies of noble gases and
471 self-potential associated with fractures and fluid dynamics in a horizontal borehole, mont
472 terri underground rock laboratory: Engineering Geology, **156**, 46 – 57.
473 Majumdar, A., and B. Bhushan, 1990, Role of fractal geometry in roughness characteriza-
474 tion and contact mechanics of surfaces: Journal of Tribology, **112**, 205–216.
475 Martinez-Pagan, P., A. Jardani, A. Revil, and A. Haas, 2010, Self-potential monitoring of
476 a salt plume: Geophysics, **75**, WA17–WA25.
477 Mauri, G., G. Williams-Jones, and G. Saracco, 2010, Depth determinations of shallow
478 hydrothermal systems by self-potential and multi-scale wavelet tomography: Journal of
479 Volcanology and Geothermal Research, **191**, 233–244.
480 Medici, G., L. West, and S. Banwart, 2019, Groundwater flow velocities in a fractured
481 carbonate aquifer-type: Implications for contaminant transport: Journal of Contaminant
482 Hydrology, **222**, 1–16.
483 Miao, T., A. Chen, Y. Xu, S. Cheng, and B. Yu, 2019, a fractal permeability model for
484 porous–fracture media with the transfer of fluids from porous matrix to fracture: Fractals,
485 **27**, 1950121.
486 Miao, T., B. Yu, Y. Duan, and Q. Fang, 2015, A fractal analysis of permeability for fractured
487 rocks: International Journal of Heat and Mass Transfer, **81**, 75 – 80.
488 Moore, J. R., and S. D. Glaser, 2007, Self-potential observations during hydraulic fracturing:
489 Journal of Geophysical Research: Solid Earth, **112**.
490 Morgan, F. D., E. R. Williams, and T. R. Madden, 1989, Streaming potential properties of
491 westerly granite with applications: Journal of Geophysical Research, **94**, 12.449–12.461.

Murphy, H. D., J. W. Tester, C. O. Grigsby, and R. M. Potter, 1981, Energy extraction from fractured geothermal reservoirs in low-permeability crystalline rock: Journal of Geophysical Research: Solid Earth, **86**, 7145–7158.

Naudet, V., A. Revil, J.-Y. Bottero, and P. Bégassat, 2003, Relationship between self-potential (sp) signals and redox conditions in contaminated groundwater: Geophysical Research Letters, **30**.

Neuman, S., 2005, Trends, prospects and challenges in quantifying flow and transport through fractured rocks: Hydrogeology Journal, **13**, 124–147.

Neuzil, C. E., and J. V. Tracy, 1981, Flow through fractures: Water Resources Research, **17**, 191–199.

Okubo, P. G., and K. Aki, 1987, Fractal geometry in the san andreas fault system: Journal of Geophysical Research: Solid Earth, **92**, 345–355.

Osiptsov, A. A., 2017, Fluid mechanics of hydraulic fracturing: a review: Journal of Petroleum Science and Engineering, **156**, 513–535.

Overbeek, J., 1952, Electrochemistry of the double layer: in colloid science, irreversible systems, h. r. kruyt, ed.: Elsevier.

Parsekian, A. D., K. Singha, B. J. Minsley, W. S. Holbrook, and L. Slater, 2015, Multiscale geophysical imaging of the critical zone: Reviews of Geophysics, **53**, 1–26.

Patterson, J. R., M. Cardiff, and K. L. Feigl, 2020, Optimizing geothermal production in fractured rock reservoirs under uncertainty: Geothermics, **88**, 101906.

Peshcherenko, A., I. Bekerov, D. Chuprakov, and D. Abdrazakov, 2022, Fast-running model for high-volume hydraulic fracturing: Journal of Petroleum Science and Engineering, **213**, 110430.

Pride, S., 1994, Governing equations for the coupled electromagnetics and acoustics of porous media: Physical Review B, **50**, 15678–15696.

Ren, F., G. Ma, Y. Wang, L. Fan, and H. Zhu, 2017, Two-phase flow pipe network method for simulation of co2 sequestration in fractured saline aquifers: International Journal of Rock Mechanics and Mining Sciences, **98**, 39–53.

Revil, A., and A. Cerepi, 2004, Streaming potentials in two-phase flow conditions: Geophysical Research Letters, **31**.

Revil, A., and P. W. J. Glover, 1998, Nature of surface electrical conductivity in natural sands, sandstones, and clays: Geophysical Research Letters, **25**, 691–694.

Revil, A., and A. Jardani, 2013, The self-potential method: Theory and applications in environmental geosciences: Cambridge University Press.

Revil, A., M. Karaoulis, T. Johnson, and A. Kemna, 2012, Review: Some low-frequency electrical methods for subsurface characterization and monitoring in hydrogeology: Hydrogeology Journal, **20**, 617–658.

Revil, A., and P. Leroy, 2004, Constitutive equations for ionic transport in porous shales: Journal of Geophysical Research: Solid Earth, **109**. (B03208).

Rice, C., and R. Whitehead, 1965, Electrokinetic flow in a narrow cylindrical capillary: J. Phys. Chem., **69**, 4017–4024.

Rod, K. A., W. Um, S. M. Colby, M. L. Rockhold, C. E. Strickland, S. Han, and A. P. Kuprat, 2019, Relative permeability for water and gas through fractures in cement: PLOS ONE, **14**, 1–17.

Roubinet, D., and J. Irving, 2014, Discrete-dual-porosity model for electric current flow in fractured rock: Journal of Geophysical Research: Solid Earth, **119**, 767–786.

Roubinet, D., J. Irving, and P. Pezard, 2018, Relating topological and electrical properties of fractured porous media: Insights into the characterization of rock fracturing: Minerals, **8**, 14.

Roubinet, D., N. Linde, D. Jougnot, and J. Irving, 2016, Streaming potential modeling in fractured rock: Insights into the identification of hydraulically active fractures: Geophysical Research Letters, **43**, 4937–4944.

Roy, A., E. Perfect, W. M. Dunne, and L. D. McKay, 2007, Fractal characterization of fracture networks: An improved box-counting technique: Journal of Geophysical Research: Solid Earth, **112**.

Roy, I. G., 2022, Subchapter 3.1 - self-potential: A low-cost geophysical method in investigating groundwater and contaminant plume, *in* Innovative Exploration Methods for Minerals, Oil, Gas, and Groundwater for Sustainable Development: Elsevier, 193–211.

Sen, P. N., and P. A. Goode, 1992, Influence of temperature on electrical conductivity on shaly sands: Geophysics, **57**, 89–96.

552 Shen, J., B. Su, and N. Guo, 2009, Anisotropic characteristics of electrical responses of
553 fractured reservoir with multiple sets of fractures: Petroleum Science, **6**, 127–138.
554 Smoluchowski, M., 1903, Contribution à la theorie de l'endosmose electrique et de quelques
555 phenomènes correlatifs: Bulletin international de l'Academie des Sciences de Cracovie,
556 **8**, 182 – 200.
557 Soueid Ahmed, A., A. Revil, S. Byrdina, A. Coperey, L. Gailler, N. Grobbe, F. Viveiros,
558 C. Silva, D. Jougnot, A. Ghorbani, C. Hogg, D. Kiyan, V. Rath, M. J. Heap, H. Grandis,
559 and H. Humaida, 2018, 3D electrical conductivity tomography of volcanoes: Journal of
560 Volcanology and Geothermal Research, **356**, 243–263.
561 Stesky, R. M., 1986, Electrical conductivity of brine-saturated fractured rock: Geophysics,
562 **51**, 1585–1593.
563 Straface, S., E. Rizzo, and F. Chidichimo, 2010, Estimation of hydraulic conductivity and
564 water table map in a large-scale laboratory model by means of the self-potential method:
565 Journal of Geophysical Research, **115**.
566 Thanh, L. D., D. Jougnot, P. V. Do, D. T. M. Hue, T. T. C. Thuy, and V. P. Tuyen, 2021,
567 Predicting electrokinetic coupling and electrical conductivity in fractured media using a
568 fractal distribution of tortuous capillary fractures: Applied Sciences, **11**.
569 Thanh, L. D., D. Jougnot, P. Van Do, and N. Van Nghia A, 2019, A physically based model
570 for the electrical conductivity of water-saturated porous media: Geophysical Journal
571 International, **219**, 866–876.
572 Thanh, L. D., D. Jougnot, P. Van Do, N. Van Nghia A, V. P. Tuyen, N. X. Ca, and N. T.
573 Hien, 2020, A physically-based model for the electrical conductivity of partially saturated
574 porous media: Geophysical Journal International.
575 Thanh, L. D., and R. Sprik, 2016, Permeability dependence of streaming potential coefficient
576 in porous media: Geophysical Prospecting, **64**, 714–725.
577 Titov, K., A. Revil, P. Konosavsky, S. Straface, and S. Troisi, 2005, Numerical modelling
578 of self-potential signals associated with a pumping test experiment: Geophysical Journal
579 International, **162**, 641–650.
580 Torabi, A., and S. S. Berg, 2011, Scaling of fault attributes: A review: Marine and
581 Petroleum Geology, **28**, 1444 – 1460.

582 Tyler, S. W., and S. W. Wheatcraft, 1990, Fractal processes in soil water retention: Water
583 Resources Research, **26**, 1047–1054.
584 Vinogradov, J., M. Hidayat, Y. Kumar, D. Healy, and J.-C. Comte, 2022a, Laboratory
585 measurements of zeta potential in fractured lewisian gneiss: Implications for the charac-
586 terization of flow in fractured crystalline bedrock: Applied Sciences, **12**.
587 Vinogradov, J., M. Hidayat, M. Sarmadivaleh, J. Derksen, D. Vega-Maza, S. Iglauer, D.
588 Jougnot, M. Azaroual, and P. Leroy, 2022b, Predictive surface complexation model of
589 the calcite-aqueous solution interface: The impact of high concentration and complex
590 composition of brines: Journal of Colloid and Interface Science, **609**, 852–867.
591 Vinogradov, J., and M. D. Jackson, 2011, Multiphase streaming potential in sandstones
592 saturated with gas/brine and oil/brine during drainage and imbibition: Geophysical Re-
593 search Letters, **38**.
594 Violay, M., P. A. Pezard, B. Ildefonse, A. Belghoul, and C. Laverne, 2010, Petrophysical
595 properties of the root zone of sheeted dikes in the ocean crust: A case study from hole
596 odp/iodp 1256d, eastern equatorial pacific: Tectonophysics, **493**, 139–152.
597 Voytek, E. B., H. R. Barnard, D. Jougnot, and K. Singha, 2019, Transpiration- and
598 precipitation-induced subsurface water flow observed using the self-potential method:
599 Hydrological Processes, **33**, 1784–1801.
600 Walsh, J., and J. Watterson, 1993, Fractal analysis of fracture patterns using the standard
601 box-counting technique: valid and invalid methodologies: Journal of Structural Geology,
602 **15**, 1509–1512.
603 Wang, J. S. Y., and J. A. Hudson, 2015, 2, *in* Fracture Flow and Underground Research
604 Laboratories for Nuclear Waste Disposal and Physics Experiments: American Geophysi-
605 cal Union (AGU), 19–41.
606 Wang, S., Y. Xu, Y. Zhang, Q. Yu, and L. Wang, 2022, Evaluating the influence of fracture
607 roughness and tortuosity on fluid seepage based on fluid seepage experiments: Applied
608 Sciences, **12**.
609 Wishart, D. N., L. D. Slater, and A. E. Gates, 2006, Self potential improves characterization
610 of hydraulically-active fractures from azimuthal geoelectrical measurements: Geophysical
611 Research Letters, **33**, L17314.

612 Zhang, C.-L., 2013, Sealing of fractures in claystone: Journal of Rock Mechanics and
613 Geotechnical Engineering, **5**, 214–220.